RSC Advances

PAPER

View Article Online
View Journal | View Issue

Cite this: *RSC Adv.*, 2024, **14**, 5617

A DFT approach to correlate the physical characteristics of novel chalcopyrites $ASbN_2$(A = Li, Na) for green technology

Junaid Munir,[a] Saif M. H. Qaid,[b] Masood Yousaf,[c] Moeen ud din,[d] Hamid M. Ghaithan,[b] Abdullah Ahmed Ali Ahmed[e] and Quratul Ain *[f]

Received 27th November 2023
Accepted 7th February 2024

DOI: 10.1039/d3ra08109e

rsc.li/rsc-advances

Semiconductor chalcopyrite compounds have been a subject of research interest due to their diverse range of physical properties that have captured the attention of scientists. In this ongoing research, we have examined the physical characteristics of $LiSbN_2$ and $NaSbN_2$ chalcopyrites using DFT. The modified Becke–Johnson (mBJ) potential is utilized for the computation of electronic structures. The stability is attained with negative formation energies and optimization curves. A bandgap of 2.60 eV in $LiSbN_2$ and 3.15 eV in $NaSbN_2$ has been achieved, which is further endorsed by the density of states. An in-depth analysis of the optical properties unveils the potential utility of $LiSbN_2$ and $NaSbN_2$ in various photovoltaic devices, attributed to its pronounced absorption in the UV spectrum. The transport characteristics are also assessed through various transport characteristics. The large electrical conductivity and *ZT* values for both chalcopyrite compounds are attained. Due to their remarkable capability to convert heat into electricity, these materials display potential for use in thermoelectric devices.

Introduction

Thermoelectric materials have gathered significant attention recently due to their extraordinary capability to transform heat into electricity and *vice versa*.[1] This property makes them essential components in various energy conversion and harvesting applications, ranging from powering spacecraft to improving the efficiency of industrial processes.[2,3] The literature suggests different classes of materials that exhibit excellent thermoelectric and optical characteristics, such as perovskites,[4–8] Zintl compounds,[9–12] Heusler alloys,[13–16] chalcogenides[17,18] and many more. In past years, there has been a developing interest in chalcopyrite-type semiconductors owing to their expanding technological use.[19] The chalcopyrite possesses two general structures, $A^{I}B^{III}C^{V}_2$ and $A^{II}B^{IV}C^{V}_2$, which are derived from II–VI and III–V semiconductors, where A and B represent cations and C denotes anion. Chalcopyrites are at the leading position of renewable energy technologies due to their capacity to become indispensable, enhance their functionality, and expand their applicability across various fields.[20,21] The chalcopyrite structure $CuInSe_2$ exhibits excellent optical properties and is used as an absorber in solar energy applications.[22] The flexibility of $Cu(In,Ga)Se_2$ makes them high efficiency solar cell materials with record efficiency of 20.8%.[23] The $AgInSe_2$ is observed to be high performance thermoelectric material with *ZT* of 1.2 at 900 K.[24] The insulating state's three-dimensional topology is observed in the potential candidate $AuInSe_2$ chalcopyrite structure.[25] The magnetic characteristics are evaluated by exercising density functional theory in the $CuFeS_2$ semiconductor with 3.64 μ_B magnetic moment.[26] The $AgGaX_2$ (X = Te, S, Se) chalcopyrite with bandgap (1.36 eV – 2.73 eV) have been studied to understand the nonlinear and linear optical effects by utilizing real space atom cutting analysis.[27] The carbon-doped $BeSi_{1-x}C_xP_2$ and $BeGe_{1-x}C_xP_2$ show improved optoelectronic (α–10^5 cm^{-1}) and related characteristics.[28] The dispersion curves of refractive index have proven the $BeSiN_2$ and $BeCN_2$ ternary compounds to possess extraordinary optical response.[29] High Seebeck coefficient is seen in n-type tin-substituted $Cu_{1-x}Sn_xFeS_2$ in comparison with p-type chalcopyrite.[30] The computed data for $CuPN_2$ with bandgap of 2.135 eV and HPN_2 with 2.4 eV bandgap shows admirable performance in terms of optical and thermoelectric attributes.[31]. There are many other Chalcopyrites such as XPN_2 (X = Na, Li)[32] $CdXP_2$ (X= Sn/Ge/Si),[33] $CuGaTe_2$,[34] $ACuS_2$(A = In, Al and Ga),[35] $LiGaX_2$ (X= S, Se, Te),[36] $Ag_{1-x}InTe_2$,[37] AgX (X = In,Ga)Te_2 (ref. 38) whose exceptional properties have been investigated. The $Cu_{1-x}InTe_2$ shows high performance in terms of thermoelectric attributes at high temperatures.[39] While existing literature has extensively

[a]*Department of Physics, Riphah International University, Lahore, Pakistan*
[b]*Department of Physics & Astronomy, College of Sciences, King Saud University, P.O. Box 2455, Riyadh 11451, Saudi Arabia*
[c]*Department of Physics, University of Education, Lahore, Pakistan*
[d]*Department of Physics, National Taiwan University, Taipei City, 10617, Taiwan*
[e]*Center for Hybrid Nanostructures (CHyN) and Fachbereich Physik, Universität Hamburg, Hamburg, 20146, Germany*
[f]*Department of Physics, University of Management and Technology, Lahore, Pakistan. E-mail: ainnie357@yahoo.com*

investigated various chalcopyrite structures, the increasing demand for environmentally sustainable technologies necessitates the exploration of additional materials with a wider range of characteristics. Enhancing the current properties of chalcopyrites or exploring novel materials with exceptional characteristics is essential for uncovering and advancing new configurations that exhibit favorable thermoelectric and optical properties. Considering the real-world applications, we intend to thoroughly investigate the structural, elastic, thermal, and optical properties of novel $LiSbN_2$ and $NaSbN_2$ chalcopyrites in the current study.

Methodology

DFT stands out as a highly effective approach within the array of computational methods employed for electronic structure calculations. DFT has acquired considerable significance in the assessment of aromaticity, the determination of electronic stability, and the analysis of molecular system dynamics.[40] The DFT calculations were performed within the Wien2k[41] package by using full-potential augmented plane wave[42] approach. Generalized gradient approximation (GGA)[43] is utilized for the computation of optimized parameters and mechanical characteristics. The inaccurate solution of exchange correlation potential with GGA leads to misleading bandgap values. The exchange correlation term is best solved with modified Becke–Johnson[44] potential, which results in precise values of bandgap and comparable to experimental data. In the calculations, the volume of unit cells is partitioned into muffin-tin spheres characterized by atomic-like wave functions, along with the remaining interstitial space. The energy eigen values converged by expanding the wave function using cutoff $R_{MT}K_{max} = 7$ in plane waves. Where R_{MT} stands for the radius of muffin-tin sphere and K_{max} represents prime K vector magnitude in the expansion of plane wave. The $l_{max} = 10$ is used inside the sphere which shows the expansion of wave function. The $G_{max} = 12$ $(a.u.)^{-1}$ was set to signify the Fourier expansion of the charge density. The total energy convergence criteria involve ensuring its stability within a margin of 0.0001 (Ryd) and achieving a charge convergence of less than 0.0001 (e $a.u.^{-3}$). A condensed mesh of 1500 K points was chosen within the irreducible Brillouin zone using the Monkhorst–Pack method. The VESTA software was used to acquire the crystal structures and Wyckoff atomic positions. The Wien2k code was employed to assess the elastic constants (C_{ij}) using the Charpin technique.[45] The BoltzTraP code is utilized to apply semi-classical Boltzmann theory using relaxation time approximation for the interpretation of thermoelectric response. The relaxation time can be evaluated using the conductivity tensor.[46]

$$\sigma_{\alpha\beta}(i,k) = e^2\tau_{i,k}\nu_\alpha(i,k)\nu_\beta(i,k) \quad (1)$$

Where $\tau_{i,k}$ is the relaxation time.

Crystal system and optimization

Chalcopyrite structures possess the general formula of ABC_2, where A and B represent cations and C is the anion. Our under investigated structures $LiSbN_2$ and $NaSbN_2$ exhibit the orthorhombic symmetry in the space group of *Pbca*. The selected Wyckoff positions for $LiSbN_2$ are Li (0.48, 0.05, 0.24), Sb (0.63, 0.94, 0.44) and N (0.78, 0.46, 0.31) and for $NaSbN_2$, these are Na (0.27, 0.28, 0.31), Sb (0.76, 0.27, 0.43), N (0.56, 0.48, 0.20). The energetically stable configuration of a structure is crucial in predicting the fundamental properties accurately and it can be achieved through structure relaxation. For this purpose, we use the optimization process to attain the ground state energies of $LiSbN_2$ and $NaSbN_2$ structures. Birch–Murnaghan equation[47] is utilized to derive the critical parameters.

$$E(V) = E_0 + \frac{9V_0B_0}{16}\left\{\left[\left(\frac{V}{V_0}\right)^{\frac{2}{3}} - 1\right]^3 B_0' + \left[\left(\frac{V}{V_0}\right)^{\frac{2}{3}} - 1\right]^2 \left[6 - 4\left(\frac{V}{V_0}\right)^{\frac{2}{3}}\right]\right\} \quad (2)$$

where V_0 is the volume at lowest energy E_0. The B′ is the pressure derivative of bulk modulus B. The crystal structures of $LiSbN_2$ and $NaSbN_2$ with corresponding optimization graphs are plotted in Fig. 1. The parabolic curves with their minimum energy points endorsed the stable phases of $LiSbN_2$ and $NaSbN_2$. The further endorsement of the stable structures and future synthesis possibilities are explored through the formation energies (E_F) calculation.

Formation energy is the energy change linked with the creation of a compound from its constituent elements, indicating the stability of the compound and is given as:

$$\boldsymbol{E_F = E_{Total} - (E_{Li/Na} + E_{Sb} + 2\ E_N)} \quad (3)$$

The total energy is given with $\boldsymbol{E_{Total}}$ and the individual element energies are $\boldsymbol{E_{Li/Na}}$, $\boldsymbol{E_{Sb}}$ and $\boldsymbol{E_N}$. The negative E_F values energetically favor the material's stability, while the positive values imply that the material's formation is not thermodynamically favored. Our calculated E_F values, as presented in Table 1, endorsed that $LiSbN_2$ and $NaSbN_2$ are more stable and likely to form under standard conditions.

Electronic structure

To analyze the energy gap and the role of electrons in various atomic orbitals, we examine the electronic band structure and the overall density of electronic states with the utilization of the mBJ potential. Additionally, it imparts valuable insights into the permissible electronic states and their associated energy levels within the material.[48,49] The band structures of $ASbN_2$(A = Li, Na) and are portrayed in Fig. 1. The $LiSbN_2$ exhibits direct band gap characterized by the valence band maximum (VBM) and conduction band minimum (CBM) residing on similar symmetry lines (Γ–Γ), with an energy difference of 2.60 eV. Substituting Li with Na leads to a higher band gap value, resulting in a new value of 3.15 eV along the symmetry lines (Γ–

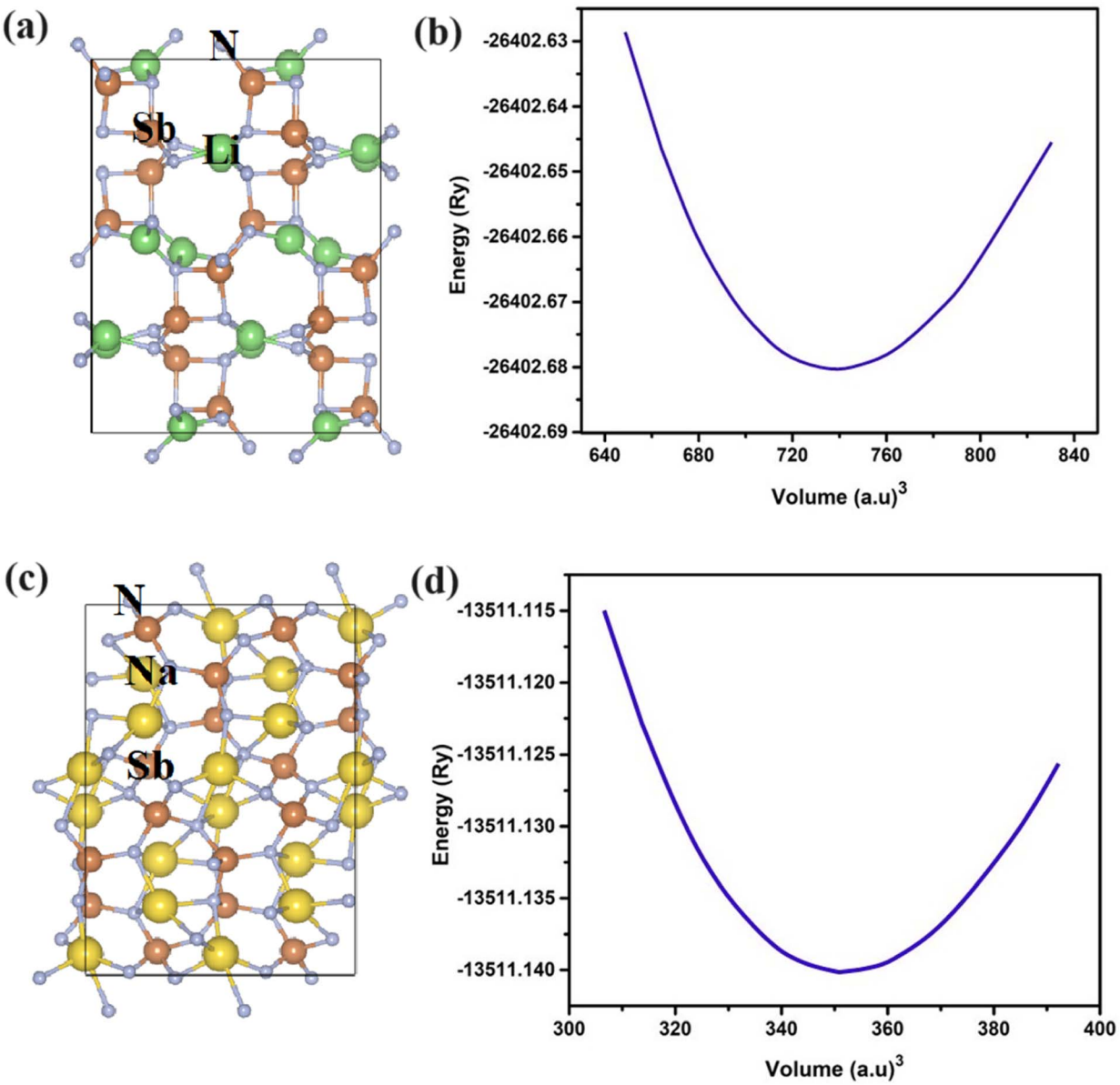

Fig. 1 The crystal structure and optimized plots of $LiSbN_2$ (a and b) and $NaSbN_2$ (c and d).

Γ). In both $LiSbN_2$ and $NaSbN_2$, the VBM intersects with the Fermi level in the band structures, suggesting that both chalcopyrites demonstrate p-type semiconductor characteristics. The importance of the distribution of electronic states becomes evident when examining the total density of states (TDOS). It acts as a significant and essential element for forecasting the physical properties of materials. The computed TDOS, depicted in Fig. 2, provides a comprehensive representation of the band structure characteristics in both chalcopyrites materials.

A precise and detailed insight into the localized electronic states can be obtained by examining the partial density of states (PTDOS). Our estimation of PTDOS allows for a comprehensive understanding of the electrical contributions, and the outcomes are illustrated in Fig. 3. For $LiSbN_2$, Sb-p and Li-s

Table 1 Lattice parameters of $LiSbN_2$ and $NaSbN_2$

Materials	Lattice constant (Å)	B (GPa)	B' (GPa)	V_o (a.u^3)	E_o (Ry)	E_F (eV per atom)
$LiSbN_2$	$a = 5.78$, $b = 11.77$, $c = 14.69$	115.5	4.6	738.055	−26402.689	−1.417
$NaSbN_2$	$a = 5.50$, $b = 11.12$, $c = 15.29$	110.3	3.6	351.45	−13511.143	−1.154

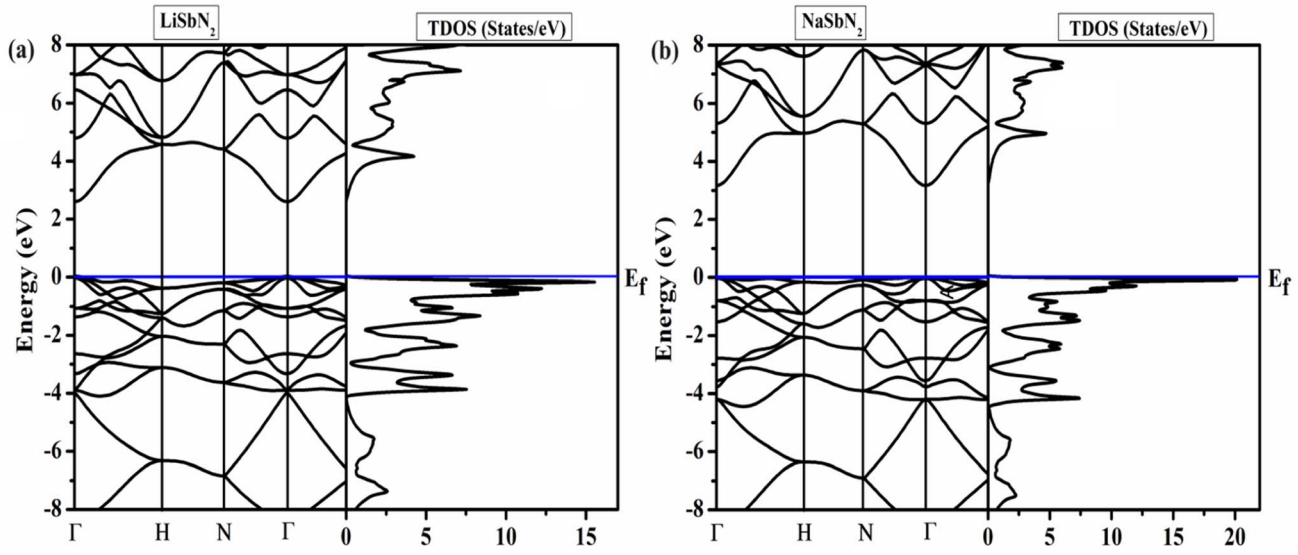

Fig. 2 (a) Band structures and (b) TDOS of $LiSbN_2$ and $NaSbN_2$.

states exhibit major effect in the valence band and small presence of N-p states. The conduction band includes the contribution of Li-s, Sb-p and N-p states. For $NaSbN_2$, Sb-p and Li-s again display their major effect in the valence band with the small presence of N-p states and the conduction band includes the role of N-p, Sb-p and Li-s states.

Optical properties

Optical characteristics are of great significance in the creation of optoelectronic devices because they enable the assessment of how a material responds to electromagnetic waves.[50] The dielectric function $\varepsilon(\omega)$ is a crucial component in explaining the optical characteristics of substances. It elucidates the manner in which a material engages with light and can be employed to compute essential optical parameters. The optical characteristics of a material are associated with its frequency due to their dependence on frequency. The $\varepsilon_1(\omega)$ governs a material's ability to store electrical energy and has a direct impact on the refractive index and plotted in Fig. 4a. The electrons within the material react to the electric field of the falling light, causing them to move away from their equilibrium positions. The charges' acceleration induces polarization, which in turn alters the speed of light as it travels through the material. The static dielectric $\varepsilon_1(0)$ function is crucial for understanding a material's response to a steady electric field. The $\varepsilon_1(0)$ value for $LiSbN_2$ is 4.4 and the substitution of Na results in the decline of $\varepsilon_1(0)$

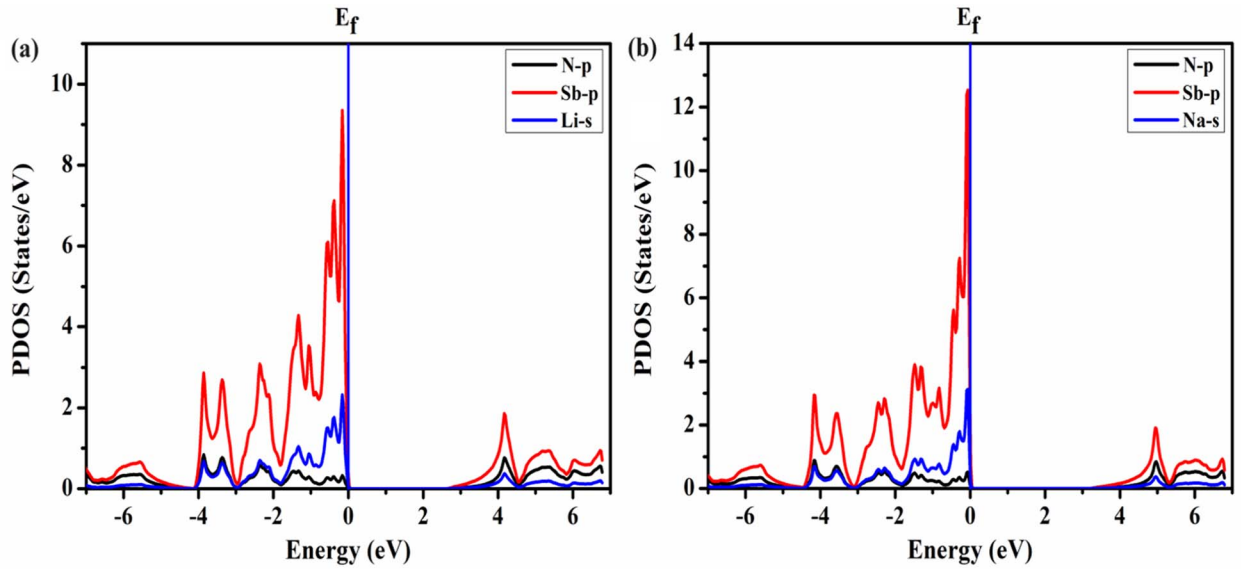

Fig. 3 PDOS of (a) $LiSbN_2$ and (b) $NaSbN_2$ chalcopyrites.

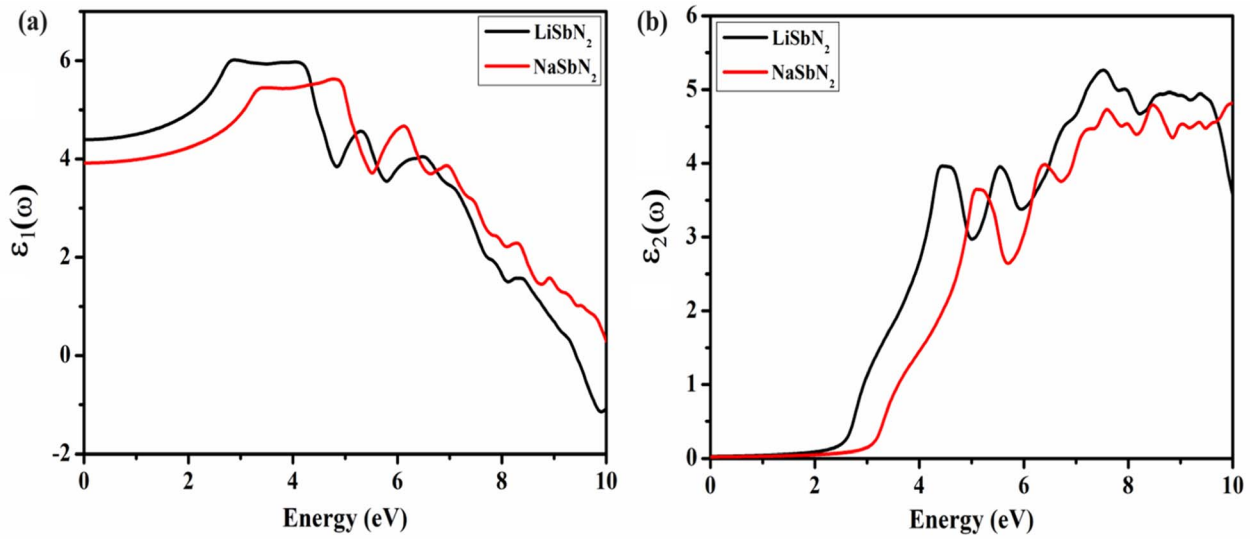

Fig. 4 The $\varepsilon_1(\omega)$ (a) and $\varepsilon_2(\omega)$ (b) for $LiSbN_2$ and $NaSbN_2$.

values and a new value of 3.9 is attained for $NaSbN_2$. For $LiSbN_2$, the initial and highest peak is detected at 2.88 eV, followed by a subsequent peak at 4.05 eV. In the case of $NaSbN_2$, the initial peak is identified at 3.45 eV, leading to the highest peak at 4.78 eV. The $\varepsilon_2(\omega)$ characterizes the absorption coefficient of the material and its capacity to interrelate with electromagnetic energy. It has a direct correlation with the electronic structure. The electronic alteration between energy states in distinct states results in the generation of the imaginary component. These electronic transitions cause the observable peaks in the $\varepsilon_2(\omega)$ curves. Fig. 4b displays the $\varepsilon_2(\omega)$ plots for $LiSbN_2$ and $NaSbN_2$. In both compounds, the initial peak arises from the transition of electrons from the valence band, mainly composed of p-states, to the conduction band, which includes both p and d-states. These peaks are photon energy dependent and also generate higher transitions. For $LiSbN_2$, the top value at 4.4 eV is observed and the substitution of Li moves the peak to the higher energy at 5.1 eV. As the energy continues to rise, additional peaks emerge due to interband transitions.

The refractive index $n(\omega)$ is a gauge of how the speed of light in a given medium compares to its speed in a vacuum. The medium's characteristics dictate the speed at which light travels through it. The $n(\omega)$ is a dimensionless ratio that illustrates how photons interact with an optical medium. It serves as a duplicate of the real part and exhibits similar behavior to $\varepsilon_1(\omega)$. The $n(\omega)$ for $LiSbN_2$ and $NaSbN_2$ is displayed in Fig. 5a. At $\omega = 0$, the $n(\omega)$ is 2.09 for $LiSbN_2$ and 1.98 for $NaSbN_2$. The first topmost value is noticed at 2.9 eV for $LiSbN_2$ and 3.5 eV for $NaSbN_2$. A small rise of energy generated the maximum values at 4.2 eV for $LiSbN_2$ and 4.8 eV for $NaSbN_2$. The absorption coefficient quantifies the extent to which a material absorbs and attenuates the intensity of incident electromagnetic radiation. A comprehensive knowledge of light absorption can be derived from the graphical representations of the absorption coefficient $\alpha(\omega)$, presented in Fig. 5b. The graphs depict the highest absorption in the UV range, while visible region also shows some absorption. The first hump is witnessed at 3.0 eV for $LiSbN_2$ and 3.5 eV for $NaSbN_2$, which lead to higher absorption peaks in UV region.

The extinction coefficient $K(\omega)$ displays a similar pattern to the imaginary component of the dielectric function and carries equivalent significance. The extinction coefficient offers valuable insights for computing the absorption of incoming photons. The plotted $K(\omega)$ values against energy are presented in Fig. 6a. The first hump is viewed at 2.9 eV for $LiSbN_2$ and 3.4 eV for $NaSbN_2$, which lead to first maxima at 4.6 eV for $LiSbN_2$ and 5.2 eV for $NaSbN_2$. The higher absorption peaks are observable in UV region. The optical loss function serves as a critical optical parameter for evaluating a material's ability to resist high-speed electrons. Minimal energy loss is observed for $LiSbN_2$ and $NaSbN_2$, as presented in Fig. 6b.

Transport characteristics

Modern power generation systems utilize thermoelectric applications to enhance the conversion of waste heat into electricity, thereby increasing overall efficiency. Thermoelectric cooling is versatile in its applications due to its ability to function without generating vibrations or noise resulting from vibrational movements. The BoltzTraP algorithm is employed to demonstrate how transport parameters are influenced at various temperature levels. The energy bands and transport characteristics are strongly interconnected with the energy level of the Fermi band. The replacement of Li with Na in the section on electronic structure leads to notable enhancements in the values of the bandgap. The bandgap primarily dictates the charge carriers involved in the transport system. Consequently, the bandgap value meaningfully influences transport parameters, for instance, conductivity and the Seebeck coefficient. To gain a deeper insight into how the bandgap influences transport characteristics, we analyzed the thermoelectric parameters using the mBJ potential. The essential parameter is the

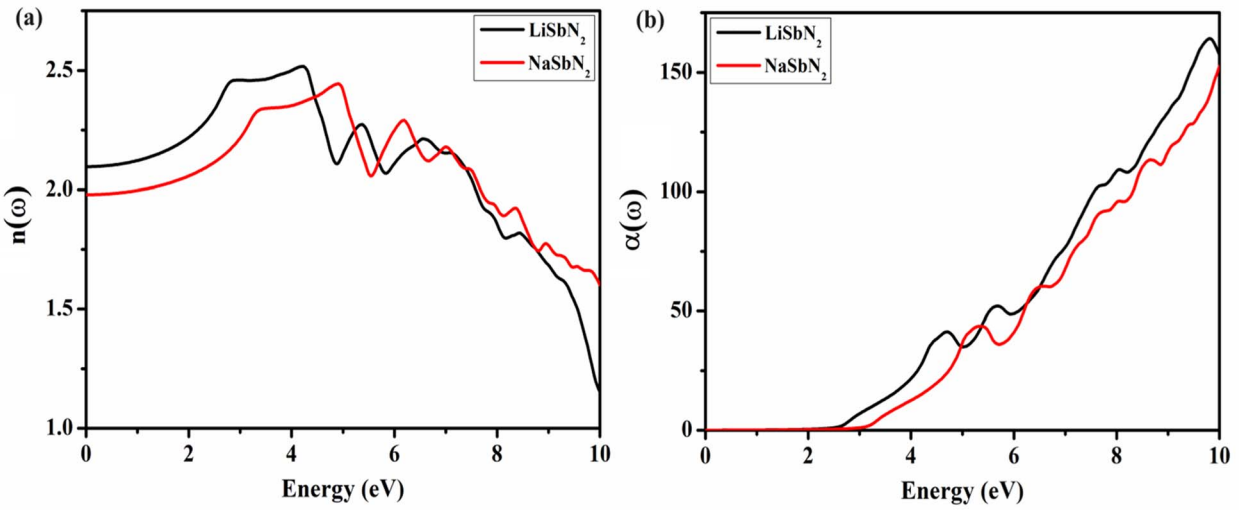

Fig. 5 The $n(\omega)$ (a) and $\alpha(\omega)$ (b) for $LiSbN_2$ and $NaSbN_2$.

electrical conductivity (σ) that is contingent on the density of charge carriers, displayed in Fig. 7a. For $LiSbN_2$, the obtained σ values are 5.33×10^{18} (S m^{-1}) at 300 K and 1.64×10^{19} (S m^{-1}) at 800 K. For $NaSbN_2$, the obtained σ values are 8.08×10^{18} (S m^{-1}) at 300 K and 1.84×10^{19} (S m^{-1}) at 800 K. A gradual increase in σ is noted as the temperature rises for both materials. The capability of a substance to transfer heat through lattice vibrations is referred to as thermal conductivity (k). The calculated electrical component pertains to the holes and electrons responsible for heat conduction. In Fig. 7b, the electronic section of thermal conductivity is illustrated as temperature gradient. The figure shows that as the temperature increases, K_{el} experiences rapid growth. For $LiSbN_2$, at 300 K, the k possesses the value of 1.14×10^{14} (Wm^{-1} K^{-1}). A gradual growth in k values is noticed beyond 300 K, resulting in an updated value of 6.64×10^{14} (Wm^{-1} K^{-1}) at 800 K. For $NaSbN_2$, the thermal conductivity possesses the value of 1.38×10^{14} (Wm^{-1} K^{-1}) at 300 K. A further growth in k values is noticed above 300 K, and at 800 K, a new value of 6.9×10^{14} (Wm^{-1} K^{-1}) is attained.

The Seebeck coefficient (S) quantifies a compound's capability to generate an electric voltage when exposed to a temperature gradient. Metals exhibit low Seebeck coefficient (S) values when compared to the high Seebeck coefficient of insulators. The Seebeck coefficient is significantly influenced by alterations in the bandgap. Seebeck coefficient is higher in band structures that are in close proximity to the Fermi level. Fig. 8a illustrates the temperature dependent Seebeck coefficient for both materials. For $LiSbN_2$, the S values are 2.31×10^{-4} (V K^{-1}) at 300 K and 1.97×10^{-4} (V K^{-1}) at 800 K. For $NaSbN_2$, the S values are

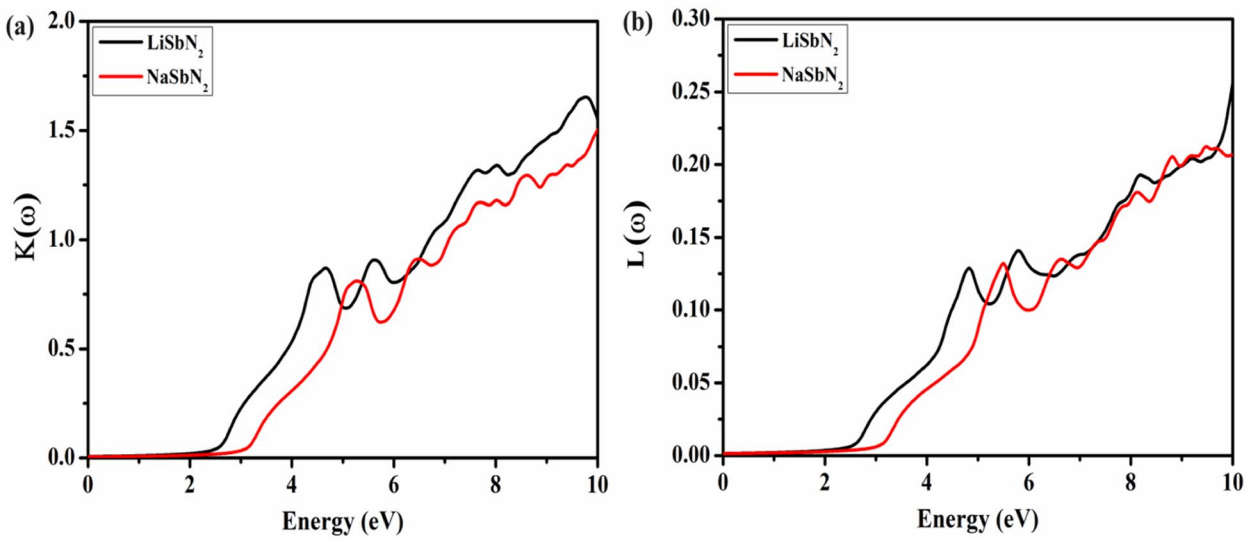

Fig. 6 Extinction coefficient (a) and $L(\omega)$ (b) for $LiSbN_2$ and $NaSbN_2$.

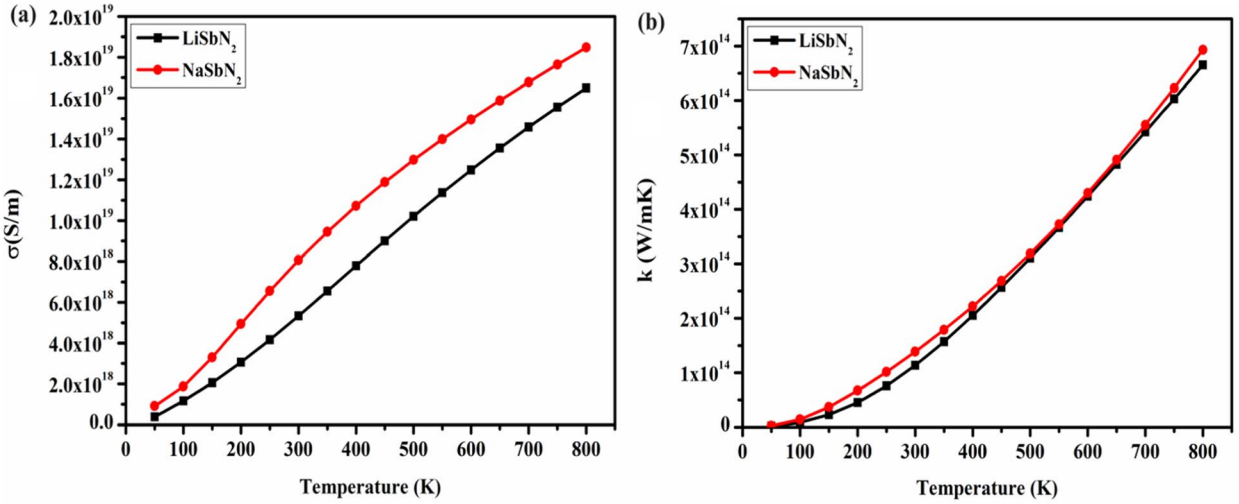

Fig. 7 Electrical (a) and thermal (b) conductivity of $LiSbN_2$ and $NaSbN_2$.

2.15×10^{-4} (V K^{-1}) at 300 K and 2.00×10^{-4} (V K^{-1}) at 800 K. The power factor (P.F.) plays a critical role in precisely assessing the potential of a thermoelectric material. The power factor is computed and plotted in the form of graphs for both materials in Fig. 8b. Growing the temperature (100–800 K) results in a gradual enhancement of the power factor (P.F.) values for both

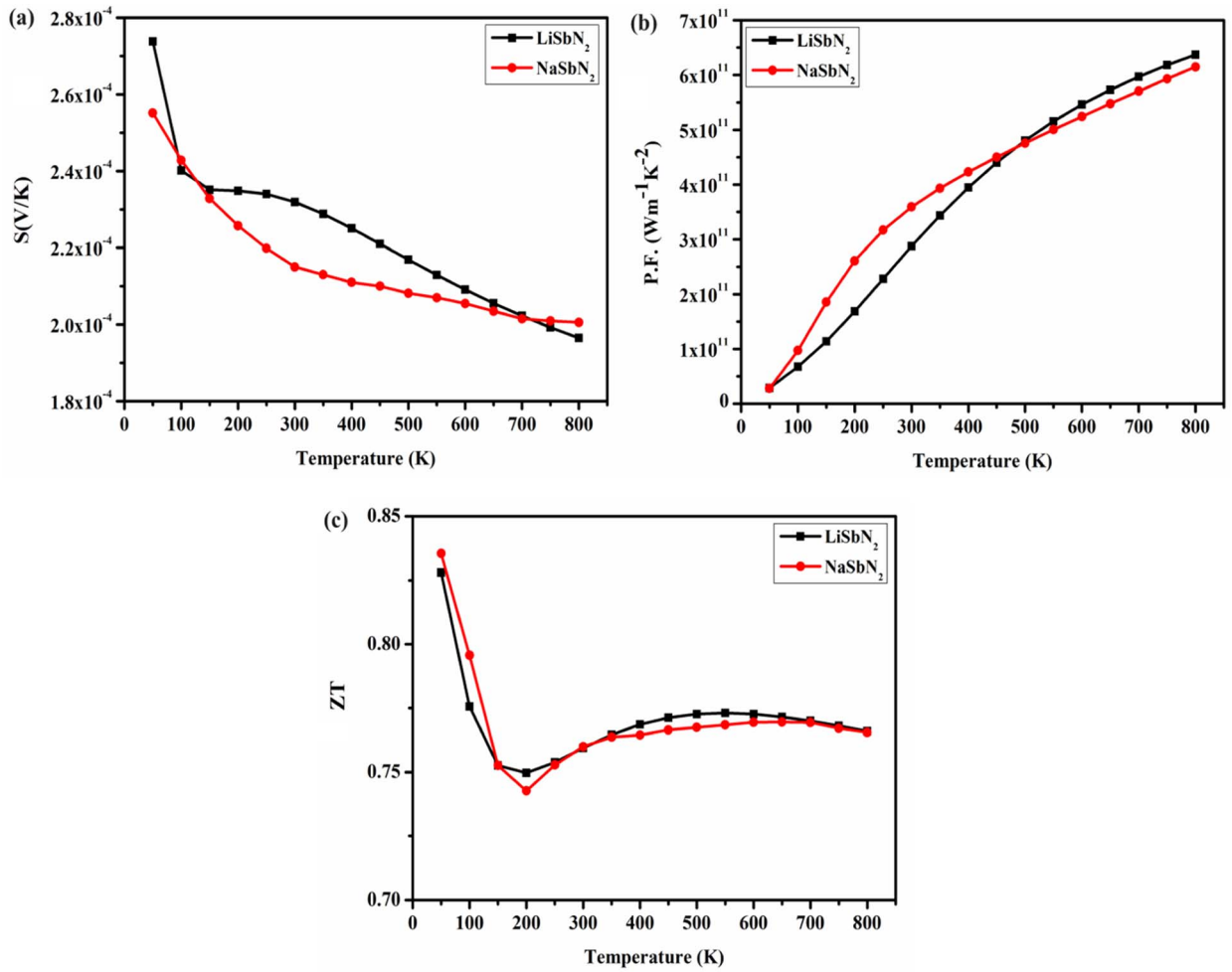

Fig. 8 The Seebeck (a), P.F (b) and *ZT* (c) of $LiSbN_2$ and $NaSbN_2$.

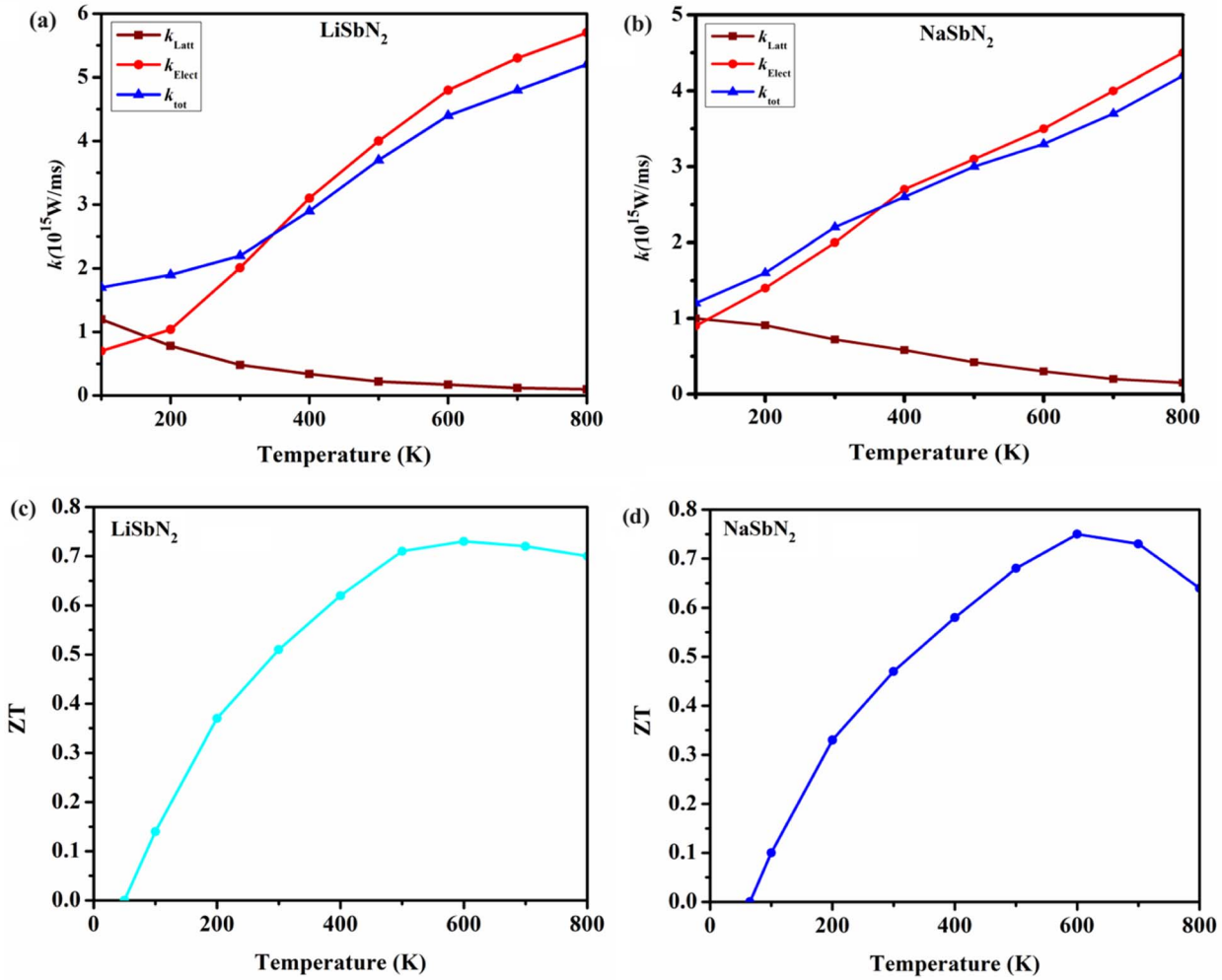

Fig. 9 Phonon dependent thermal conductivity and *ZT* of $LiSbN_2$ (a and c) and $NaSbN_2$ (b and d).

chalcopyrites. At 300 K, the P.F has the value of 2.87×10^{11} (Wm^{-1} K^{-2}), which increases to 6.37×10^{11} (Wm^{-1} K^{-2}) at 800 K for $LiSbN_2$. For $NaSbN_2$, the P.F is noted as 3.58×10^{11} (Wm^{-1} K^{-2}) at 300 K that further rises to 6.14×10^{11} (Wm^{-1} K^{-2}) at 800 K.

The figure of merit (*ZT*) is a vital parameter in thermoelectric materials, serving as a fundamental measure of the material's effectiveness in transforming heat into electrical energy. A higher *ZT* value signifies a more efficient thermoelectric material, as it combines aspects like the Seebeck coefficient, electrical conductivity, and thermal conductivity to evaluate performance in energy conversion applications. The *ZT* for $LiSbN_2$ and $NaSbN_2$ is plotted in Fig. 8c. For $LiSbN_2$, *ZT* possesses a value of 0.83, at 50 K, which shows a drop to 200 K with a value of 0.75. After 200 K, a gradual rise is noticed in *ZT* and it has 0.76 values at 300 K. This increase in *ZT* continuous until 800 K, where it possesses the value of 0.77. For $NaSbN_2$, the same trend is observed as in $LiSbN_2$. At 50 K, the *ZT* is 0.84, which reduces to 0.74 at 200 K. At 300 K, it is 0.76 and at 800 K, it is 0.77. The significant electrical conductivity and Seebeck values observed in both chalcopyrites, coupled with their impressive *ZT* values, provide strong support for considering $LiSbN_2$ and $NaSbN_2$ as promising candidates for renewable energy applications.

In addition, the combined effect of thermal conductivity containing electronic and lattice thermal conductivities are evaluated and presented in Fig. 9a and b. The lattice vibrations shows a decreasing trend with the temperature rise and simultaneously, the electronic part and total thermal conductivity shows an increasing trend for $LiSbN_2$ and $NaSbN_2$. It can be concluded from the graphs that electronic part plays a major role in thermal conductivity. Furthermore, the phonon dependent *ZT* values for $LiSbN_2$ and $NaSbN_2$ are also computed and presented in Fig. 9c and d. A sharp rise in the value of *ZT* is noticed after 50 K for both materials. The *ZT* highest value of 0.73 (600 K) for $LiSbN_2$ and 0.75 (600 K) for $NaSbN_2$ is achieved. After 600 K, a small decline is noticed in the *ZT* values of $LiSbN_2$ and $NaSbN_2$.

Conclusion

The physical characteristics of $LiSbN_2$ and $NaSbN_2$ are assessed using the FP-LAPW method incorporated within the Wein2K code. The stability of materials was convincingly established

through an analysis of the volume optimization curve and formation energy. The confirmation of their semiconductor character is based on the computed electronic bandgap and the overall DOS. A comprehensive examination of the optical characteristics unveiled their suitability for use in photovoltaic technology. At 800 K, a *ZT* of 0.77 is attained for both materials, indicating their potential suitability for consumption in thermoelectric devices.

Data availability

Data will be made available on request.

Conflicts of interest

There is no conflicts to declare.

Acknowledgements

The authors extend their appreciation to the Deputyship for Research and Innovation, Ministry of Education in Saudi Arabia for funding this research work through the project no. (IFKSUOR3–073–16).

References

1 J. R. Sootsman, D. Y. Chung and M. G. Kanatzidis, New and old concepts in thermoelectric materials, *Angew. Chem., Int. Ed.*, 2009, **48**(46), 8616–8639.
2 L. Yang, *et al.*, High performance thermoelectric materials: progress and their applications, *Adv. Energy Mater.*, 2018, **8**(6), 1701797.
3 L. Zhang, *et al.*, Flexible thermoelectric materials and devices: From materials to applications, *Mater. Today*, 2021, **46**, 62–108.
4 J. Munir, *et al.*, First-principles investigations of the mechanically and thermodynamically stable potassium-based double perovskites K_2TlAsX_6 (X= Cl, Br) for optoelectronic and renewable applications, *J. Mater. Sci. Eng. B*, 2023, **298**, 116830.
5 S. M. Qaid, *et al.*, A computational insight into Rb_2ASbX_6 (A= Tl, Cu & X= I, Cl) double perovskites for energy storage and optoelectronic applications, *Phys. Scr.*, 2023, **98**(10), 105910.
6 M. U. Din, *et al.*, Scrutinized the spin-orbit coupling effect on the elastically and thermodynamically stable $Rb2BCl_6$ (B= Pb, Ti) double perovskites for photocatalytic, optoelectronic and renewable energy applications, *Mater. Sci. Semicond. Process.*, 2023, **163**, 107569.
7 J. Munir, *et al.*, Electronic structure and optical and thermoelectric response of lead-free double perovskite $BaMgLaBiO_6$: a first-principles study, *J. Comput. Electron.*, 2023, 1–13.
8 J. Munir, *et al.*, Physical properties of elastically and thermodynamically stable magnetic $AcXO_3$ (X= Cr, Fe) perovskite oxides: a DFT investigation, *Phys. Scr.*, 2023, **98**(6), 065513.
9 Q. Ain, H. Ullah and J. Munir, Structural, optoelectronic and thermal response of new stable $MgBe_2X_2$ (X= As, P) Zintl phases: First-principles calculation, *J. Mater. Sci. Eng. B*, 2023, **287**, 116136.
10 K. Fatima, *et al.*, Ground state electronic structure, optical and thermoelectric response of Zintl phase $MgAl_2X_2$ (X= C, Sb) for renewable energy applications, *Phys. B*, 2022, **631**, 413688.
11 J. Munir, *et al.*, An insight into the electronic, optical and transport properties of promising Zintl-phase $BaMg_2P_2$, *Phys. B*, 2021, **618**, 413181.
12 J. Munir, *et al.*, A computational insight into the Zintl SZr_2N_2 and $BaAg_2S_2$ phases for optoelectronic thermoelectric applications, *Phys. B*, 2023, **671**, 415403.
13 Q. Ain, *et al.*, A promising optoelectronic and thermoelectric response of full Heusler Na2TlX (X= Bi, Sb) alloys: A DFT approach, *Phys. Scr.*, 2023, **98**, 115920.
14 F. Firdous, *et al.*, Half-metallicity, magnetic and optical attributes of mechanically stable half-Heusler VSnX (X= Pt, Pd) alloys for spintronics: a DFT study, *Eur. Phys. J. Plus*, 2023, **138**(8), 699.
15 Q. Ain, *et al.*, Electromagnetic, optical and thermoelectric response of full-Heusler Co_2VGe alloy for spintronic and thermoelectric applications: DFT+ SOC study, *Phys. B*, 2023, **657**, 414820.
16 Q. Ain, *et al.*, First-principles analysis of the physical properties of XAcTe2 (X= Li, Na) Heusler alloys for optoelectronic and thermoelectric devices, *Comput. Mater. Sci.*, 2023, **224**, 112156.
17 M. Nadeem, *et al.*, Exploring the physical properties of Cu2WSe4 for optoelectronic and thermoelectric applications: a DFT study, *ECS J. Solid State Sci. Technol.*, 2022, **11**(3), 033009.
18 Y. Shi, C. Sturm and H. Kleinke, Chalcogenides as thermoelectric materials, *J. Solid State Chem.*, 2019, **270**, 273–279.
19 S. Das, *et al.*, Structure, electronic and optical properties of chalcopyrite-type semiconducting materials $XGaY_2$ (X= Cu, Ag, Au; Y= S, Se, Te) for solar cell applications: a DFT study, *Phys. B*, 2022, **646**, 414305.
20 K. Khan, *et al.*, First principle study of optical and electronic response of Ca-based novel chalcopyrite compounds, *Phys. Scr.*, 2023, **98**(3), 035821.
21 H. Xie, *et al.*, High Thermoelectric Performance in Chalcopyrite $Cu_{1-x}Ag_x$ $GaTe_2$–ZnTe: Nontrivial Band Structure and Dynamic Doping Effect, *J. Am. Chem. Soc.*, 2022, **144**(20), 9113–9125.
22 A. R. Uhl, *et al.*, Liquid-selenium-enhanced grain growth of nanoparticle precursor layers for $CuInSe_2$ solar cell absorbers, *Prog. Photovoltaics*, 2015, **23**(9), 1110–1119.
23 R. Carron, *et al.*, Advanced alkali treatments for high-efficiency Cu (In, Ga) Se_2 solar cells on flexible substrates, *Adv. Energy Mater.*, 2019, **9**(24), 1900408.
24 S. Huang, *et al.*, High Performance of N-type thermoelectric Material $AgInSe_2$ Originated from Strong Acoustic Phonon Scattering, *Mater. Lab.*, 2023, **2**, 1–7.

25 W. Feng and Y. Yao, Three-dimensional topological insulators: A review on host materials, *Sci. China: Phys., Mech. Astron.*, 2012, **55**, 2199–2212.
26 M. Zhou, *et al.*, Structural, electronic, and elastic properties of $CuFeS_2$: first-principles study, *Appl. Phys. A*, 2015, **118**, 1145–1152.
27 L. Bai, *et al.*, Mechanism of linear and nonlinear optical effects of chalcopyrite $AgGaX_2$ (X= S, Se, and Te) crystals, *J. Chem. Phys.*, 2004, **120**(18), 8772–8778.
28 F. Mekkaoui, *et al.*, Insight into physical properties of carbon-doped BeSiP2 and $BeGeP_2$ chalcopyrite: An *ab initio* study, *J. Solid State Chem.*, 2023, **323**, 124054.
29 T. Dahame, *et al.*, Electronic, elastic, linear and nonlinear optical properties of beryllium based chalcopyrite $BeMN_2$ (M= C, Si): An *ab initio* study, *Phys. B*, 2019, **561**, 37–42.
30 S. Tippireddy, *et al.*, Tin-substituted chalcopyrite: an n-type sulfide with enhanced thermoelectric performance, *Chem. Mater.*, 2022, **34**(13), 5860–5873.
31 T. Ghellab, *et al.*, Ab initio full-potential study of the fundamental properties of chalcopyrite semiconductors XPN_2 (X= H, Cu), *Mater. Res. Express*, 2019, **6**(7), 075906.
32 T. Ghellab, *et al.*, Structural, elastic, electronic and thermoelectric properties of XPN_2 (X= Li, Na): First-principles study, *Int. J. Mod. Phys. B*, 2019, **33**(21), 1950234.
33 N. Megag, *et al.*, Band parameters and thermoelectric properties of chalcopyrite ternary compounds $CdXP_2$ (X= Si, Ge and Sn), *Comput. Condens. Matter*, 2021, **28**, e00577.
34 T. Plirdpring, *et al.*, Chalcopyrite $CuGaTe_2$: a high-efficiency bulk thermoelectric material, *Adv. Mater.*, 2012, **24**(27), 3622–3626.
35 I. Ghazal, *et al.*, Investigation of the electronic, structural, optical and thermoelectric properties of ternary chalcopyrite $ACuS_2$ (A= Al, Ga and In): *Ab initio* study, *Optik*, 2022, **260**, 169077.
36 M. Yaseen, G. Murtaza and R. M. A. Khalil, Ab-initio study of Li based chalcopyrite compounds $LiGaX_2$ (X= S, Se, Te) in tetragonal symmetry: A class of future materials for optoelectronic applications, *Curr. Appl. Phys.*, 2018, **18**(10), 1113–1121.
37 Y. Aikebaier, *et al.*, High-temperature thermoelectric properties of non-stoichiometric $Ag_{1-x}InTe_2$ with chalcopyrite structure, *J. Mater. Sci. Eng. B*, 2012, **177**(12), 999–1002.
38 J. Yang, Q. Fan and X. Cheng, Prediction for electronic, vibrational and thermoelectric properties of chalcopyrite AgX (X= In, Ga) Te_2: PBE+ U approach, *R. Soc. Open Sci.*, 2017, **4**(10), 170750.
39 A. Kosuga, *et al.*, High-temperature thermoelectric properties of $Cu_{1-x}InTe_2$ with a chalcopyrite structure, *Appl. Phys. Lett.*, 2012, **100**(4), 042108.
40 M. Orio, D. A. Pantazis and F. Neese, Density functional theory, *Photosynth. Res.*, 2009, **102**, 443–453.
41 P. Blaha, et al., *wien2k. An augmented plane wave+ local orbitals program for calculating crystal properties*, 2001.
42 M. Petersen, *et al.*, Improving the efficiency of FP-LAPW calculations, *Comput. Phys. Commun.*, 2000, **126**(3), 294–309.
43 Z. Wu and R. E. Cohen, More accurate generalized gradient approximation for solids, *Phys. Rev. B*, 2006, **73**(23), 235116.
44 D. Koller, F. Tran and P. Blaha, Improving the modified Becke–Johnson exchange potential, *Phys. Rev. B*, 2012, **85**(15), 155109.
45 A. Bouhemadou, *et al.*, FP-APW+ lo calculations of the elastic properties in zinc-blende III-P compounds under pressure effects, *Comput. Mater. Sci.*, 2009, **45**(2), 474–479.
46 G. K. Madsen and D. J. Singh, BoltzTraP. A code for calculating band-structure dependent quantities, *Comput. Phys. Commun.*, 2006, **175**(1), 67–71.
47 T. Katsura and Y. Tange, A simple derivation of the Birch–Murnaghan equations of state (EOSs) and comparison with EOSs derived from other definitions of finite strain, *Minerals*, 2019, **9**(12), 745.
48 H. Murtaza, *et al.*, Exploring the optoelectronic attributes, thermoelectric and photocatalytic potential of double perovskites $Cs_2BB'H_6$ (B= Al, Na and B′= Tl, In): A DFT study, *J. Mater. Sci. Eng. B*, 2024, **301**, 117171.
49 H. Murtaza, *et al.*, Scrutinize the physical attributes of thermodynamically and elastically stable double perovskite oxides Ba_2CdXO_6 (X= Mo, U) for optoelectronics, photocatalytic and green technology, *Comput. Mater. Sci.*, 2024, **232**, 112674.
50 S. M. Qaid, *et al.*, First-principles investigations on the structural, optoelectronic, mechanical and transport properties of new stable lead-free double perovskites Cs2BB′ I6 (B= Ag/Rb, B′= Bi/Ga) halides, *J. Mater. Sci. Eng. B*, 2024, **301**, 117176.